

Machine learning and a computational fluid dynamic approach to estimate phase composition of chemical vapor deposition boron carbide

Qingfeng Zeng^{a,e*}, Yong Gao^a, Kang Guan^{b*}, Jiantao Liu^c, Zhiqiang Feng^{c,d}

^a *Science and Technology on Thermostructural Composite Materials Laboratory, School of Materials Science and Engineering, Northwestern Polytechnical University, Xi'an 710072, China*

^b *School of Materials Science and Engineering, South China University of Technology, Guangzhou 510640, China*

^c *School of Mechanical Engineering, Southwest Jiaotong University, Chengdu, China*

^d *Evry University, Paris, France*

^e *MSEA International Institute for Materials Genome, Gu'an 065500, Hebei, China*

* Corresponding author. E-mail address: qfzeng@nwpu.edu.cn (Q. Zeng).

* Corresponding author. E-mail address: mskguan@scut.edu.cn (K. Guan).

Abstract

Chemical vapor deposition is an important method for the preparation of boron carbide. Knowledge of the correlation between the phase composition of the deposit and the deposition conditions (temperature, inlet gas composition, total pressure, reactor configuration, and total flow rate) has not been completely determined. In this work, a novel approach to identify the kinetic mechanisms for the deposit composition is presented. Machine learning (ML) and computational fluid dynamic (CFD) techniques are utilized to identify core factors that influence the deposit composition. It has been shown that ML, combined with CFD, can reduce the prediction error from 25% to 7%, compared with the ML approach alone. The sensitivity coefficient study shows that BHCl_2 and BCl_3 produce the most boron atoms, while C_2H_4 and CH_4 are the main sources of carbon atoms. The new approach can accurately predict the deposited boron-carbon ratio and provide a new design solution for other multi-element systems.

Key words: machine learning; computational fluid dynamic; chemical vapor deposition; boron carbide; B/C ratio; kinetic mechanisms

1 Introduction

Ceramic matrix composite (CMC) is an ideal high-temperature material because of its high-temperature resistance, wear resistance, low thermal conductivity, low thermal expansion coefficient, high chemical resistance, and high strength [1, 2]. The common material systems of CMC are carbon fiber-reinforced silicon carbide ceramic matrix composite and silicon carbide fiber-reinforced silicon carbide ceramic matrix composite (C_f/SiC and SiC_f/SiC) [3-5]. Because boron carbide (B_xC) can react with oxygen to generate boron oxide glass phase (B_2O_3 , HBO_3 and H_3BO_3) and then seal cracks to prevent further oxidation [6-9], it is a good candidate for oxidation protective materials, and it is usually added to modify the interface and matrix of CMC.

Chemical vapor deposition (CVD) is a promising method for the preparation of boron carbide [7, 10-12]. The deposition mechanism for B_xC from a $BCl_3-CH_4-H_2$ system has been previously studied. For instance, Berjonneau et al. identified the main gaseous species in situ by FTIR spectrometry as BCl_3 , $BHCl_2$, and HCl [13, 14]. The B/C ratio of the deposits decreased from 3.6 to 2 when the deposition temperature increased from 900 °C to 1100 °C. Karaman et al. considered $BHCl_2$ a by-product of the gas phase [11, 12]. Liu et al. systematically studied the relationship between deposition morphology and processing conditions [15]. They found that temperature has an effect on the phase composition and microstructure. At higher temperature (1050 °C–1100 °C), the deposit consisted of two interlaced phases (PyC and boron carbide) with low boron content ranging from about 40–49 at.%. At lower temperature (900 °C–950 °C), layered and dense B_4C was produced with uniform phase composition, and its boron content is 65–79 at.%.

It was considered that B_xC exists as a single stable phase in a large homogeneous region from about 8 to 20 at.% carbon concentration (the corresponding B/C ratio is from 11.5 to 4) [7], and then a carbon-rich B_xC coating was obtained when B/C ratio was lower than 4 [15, 16]. Thus, it is important to elucidate the correlation between

the B/C ratio of the deposit and the deposition conditions to achieve reproducibility and consistency in the process. Apart from experimental studies, some numerical studies have provided an in-depth understanding of deposition kinetics [17-19], but no modeling attempts have been reported in boron carbide.

This paper is concerned with the correlation between deposit composition and processing parameters, such as temperature, inlet gas concentration, pressure, and gas flow velocity. A novel approach that considers gas phase kinetics and heat and mass transfer, in combination with machine learning (ML), is proposed to better understand the actual deposition mechanism and design of the deposit composition. The approach was applied to a $\text{BCl}_3\text{-CH}_4\text{-H}_2$ system, which provides a useful foundation in understanding other precursor systems, such as $\text{SiCl}_4\text{-BCl}_3\text{-NH}_3\text{-H}_2\text{-Ar}$ [20] and $\text{BCl}_3\text{-MTS-H}_2$ [13].

This paper is organized as follows: In the second section, the details of the reactor model (RM) and two machine learning methods (ML), including error back propagation algorithm (BP) and support vector machine (SVM), are presented. In the third section, ML was used to directly correlate the global processing parameters (temperature, inlet gas composition, total pressure, reactor inner diameter, and total flow rate) with the experimentally measured boron-carbon ratio of the deposits. However, no satisfactory functional relationship was found. Then, the proposed method was applied and validated by comparing the experimental data.

2. Model simulation and prediction

2.1 Reactor-scale model (RM)

The experimental data reported by Liu and Berjonneau are adopted in this study [13-15]. The specific deposition parameters for their experiments are listed in Table 1. In Liu's experiments, B_4C and pyrogenation carbon (PyC) were deposited onto graphite slices (30 mm \times 15 mm \times 2 mm) [15]. Boron trichloride ($\text{BCl}_3 \geq 99.99$ vol.%) and methane ($\text{CH}_4 \geq 99.95$ vol.%) were used as the boron and carbon sources, respectively. The reactor was a vertical, hot-wall deposition furnace with a 200 mm inner diameter (a diagram of the equipment is shown in Figure 1). The temperature

within the reactor was 900 °C - 1100 °C, and the pressure was fixed at 10 kPa. Berjonneau et al. adopted the analogous CVD reactor, which was a vertical silica glass tube (700 mm length and 34 mm internal diameter) heated in its central part by a radio-frequency induction furnace. Their processing conditions are as follows: 850 °C–1000 °C, 2–12 kPa, and total flow rate of 210–390 sccm.

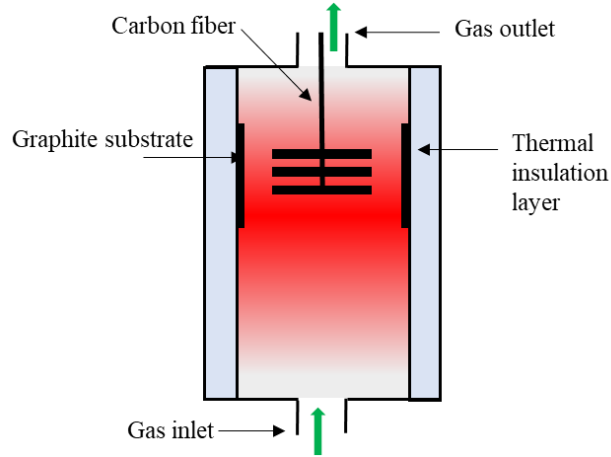


Fig 1. CVD reactor equipment diagram.

Table 1. CVD experimental conditions from references [13-15]

Number	T/ °C	Q/sccm	ID/mm	P/kPa	In_BCl ₃	In_CH ₄	In_H ₂	B/C
1	900	125	200	10	10/23	2/23	11/23	4.34
2	900	125	200	10	2/19	2/19	15/19	0.31
3	900	125	200	10	2/5	2/15	11/15	4.70
4	950	125	200	10	8/23	2/23	13/23	2.31
5	950	125	200	10	4/15	2/15	9/15	1.83
6	950	125	200	10	8/21	2/21	11/21	0.99
7	1000	125	200	10	2/11	2/11	7/11	0.35
8	1000	125	200	10	4/19	2/19	13/19	0.42
9	1000	125	200	10	10/27	2/27	15/27	2.32
10	1050	125	200	10	6/17	2/17	9/17	0.91
11	1050	125	200	10	4/19	2/19	13/19	0.70
12	1050	125	200	10	8/19	2/19	9/19	0.84
13	1100	125	200	10	6/23	2/23	15/23	0.78
14	1100	125	200	10	10/19	2/19	7/19	0.98

15	1100	125	200	10	2/15	2/15	11/15	0.44
16	850	250	34	12	4/25	1/25	20/25	3.5
17	900	250	34	12	4/25	1/25	20/25	2.8
18	950	250	34	12	4/25	1/25	20/25	2.8
19	850	390	34	12	2/13	1/13	10/13	3.6
20	900	390	34	12	2/13	1/13	10/13	3.0
21	950	390	34	12	2/13	1/13	10/13	3.2
22	1000	390	34	12	2/13	1/13	10/13	2.0
23	850	390	34	12	4/13	1/13	8/13	2.9
24	900	390	34	12	4/13	1/13	8/13	3.1
25	950	390	34	12	4/13	1/13	8/13	2.6
26	850	210	34	12	2/7	1/7	4/7	2.4
27	900	210	34	12	2/7	1/7	4/7	2.3
28	950	210	34	12	2/7	1/7	4/7	2.9

Here, T is deposition temperature, and Q is total flow rate. In_BCl₃, In_CH₄ and In_H₂ are the input molar fraction of BCl₃, CH₄, and H₂, respectively. ID is reactor inner diameter, P is the total pressure, and B/C is the boron-carbon ratio of the deposited products.

Because the reactor is cylindrical and symmetrical, the model can be simplified to a two-dimensional axisymmetric model. The mass and heat transfer values were accounted via conservation of mass and conservation of momentum:

$$\nabla \cdot (\rho \mathbf{u}) = 0, \quad (1)$$

$$\rho(\mathbf{u} \cdot \nabla) \mathbf{u} = \nabla \cdot [-p\mathbf{I} + \mu \left(\nabla \mathbf{u} + (\nabla \mathbf{u})^T - \frac{2}{3} \mu (\nabla \cdot \mathbf{u}) \mathbf{I} \right)]. \quad (2)$$

Here p is the fluid pressure; μ is the hydrodynamic viscosity; ρ is the fluid density; \mathbf{u} is the fluid velocity field; T is the temperature of the fluid; and \mathbf{I} is unit tensor.

The chamber was heated through the induction of the graphite layer by the RF coil to generate eddy currents. Heat transfer occurred mainly through surface radiation and convection conduction, and electromagnetic phenomenon was neglected. The main governing equations are as follows:

$$\rho C_p \mathbf{u} \cdot \nabla T + \nabla \cdot \mathbf{q} = Q. \quad (3)$$

Here, C_p is the fluid heat capacity; Q is the heat source; and \mathbf{q} is the Fourier heat conduction.

For multi-component diffusion,

$$\nabla \cdot \left(-\rho D_i \nabla Y_i - D_i^T \nabla (\ln T) \right) + \rho (\mathbf{u} \cdot \nabla) Y_i = R_i. \quad (4)$$

Here, R_i is reaction rate; Y_i is mass fraction; D_i is the binary diffusion coefficient between i th species and hydrogen; and D_i^T is thermal diffusivity. The following formula was used to calculate the binary diffusion rate (m^2/s):

$$D_i = 2.695 \cdot 10^{-3} \cdot \frac{\sqrt{T^3 ((M_A + M_B) / (2 \cdot 10^3 M_A M_B))}}{p \sigma_A \sigma_B \Omega_D}, \quad (5)$$

where M is molar mass; σ is the minimum energy values of the characteristic length; p is pressure; subscripts A and B indicate binary diffusion gas species; and Ω_D is the collision integral:

$$\Omega_D = f \left(T, \sigma, \frac{\varepsilon}{k_b}, \mu_D \right). \quad (6)$$

To calculate the collision integral Ω_D , we need to define the minimum energy values of the characteristic length and Lennard–Jones interaction potential, which are σ (10^{-10} m) and ε/k_b (K), respectively. It is also necessary to provide a material dipole moment μ_D (Debye). The values were obtained from previous works [21], databases, or experiments (Table 2). σ and ε/k_b of BCl_3 were approximated for the unknown coefficients of other boron-containing intermediates.

Table 2. Characteristic lengths of major substances (ε/k_b) and Lennard-Jones interaction potential (σ)

Gas species	(ε/k_b) (K)	σ (Å)
CH_4	154	3.78
C_2H_2	209	4.1
C_2H_4	280	3.97
C_2H_6	252.3	4.302
HCl	344.7	3.339
H_2	38	2.92
BCl_3	337.7	5.127

Here, the material dipole moment μ_D is uniformly zero.

The detailed chemical kinetic model that describes gas-phase reactions in CVD has been presented in several studies. Table 3 lists 62 reversible reactions adopted for the gas model in the present case. Ge et al. [22-24] focused precisely on the thermodynamics of Si-C-H -Cl systems. Moreover, the temperature conditions they studied are within the range of our research temperature. Therefore, for C-H -Cl systems (G1-G44 in Table 3), we preferentially adopted Ge's calculated data. Based on the most favorable reaction path previously proposed, Su et al. studied the reaction rate of the BCl₃/CH₄/H₂ gas-phase system [25]. Their rate constants were calculated for temperatures within 200–2000 K and adopted here (G45-G58) [26]. Reinisch et al. reported a set of theoretical experiments of the gas-phase decomposition of boron trichloride in the presence of hydrogen radicals [27], and their reactions are also included (G59-G62 in Table 3).

Table 3. A list of gas phase reaction models

No	Reaction	A (s^{-1} or $m^3 mol^{-1} s^{-1}$)	n	E ($kJ mol^{-1}$)
G1	CH ₄ →CH ₃ + H	8.3×10^{13}	0	434.4
	reverse rate	1.294×10^9	-0.4	0
G2	C ₂ H ₄ →C ₂ H ₂ + H ₂	5.317×10^{11}	0.892	454.7
	reverse rate	430.4	1.273	271.2
G3	C ₂ H ₅ →C ₂ H ₄ + H	1.66×10^{13}	0.093	171.5
	reverse rate	9.834×10^7	0.098	30.1
G4	C ₂ H ₆ →2CH ₃	1.2×10^{22}	-1.79	381
	reverse rate	1.024×10^9	-0.64	0
G5	C ₂ H ₆ + CH ₂ ↔C ₂ H ₅ + CH ₃	1.2×10^8	0	0
G6	2CH↔C ₂ H ₂	1.204×10^8	0	0
G7	CH ₂ + H↔CH + H ₂	3.011×10^7	0	0
G8	CH ₂ + CH↔C ₂ H ₂ + H	3.975×10^7	0	0
G9	2CH ₂ ↔C ₂ H ₄	1.024×10^6	0	0
G10	2CH ₂ ↔C ₂ H ₂ + 2H	1.084×10^8	0	3.3
G11	2CH ₂ ↔C ₂ H ₂ + H ₂	1.204×10^7	0	3.3
G12	CH ₃ + CH↔C ₂ H ₃ + H	3.011×10^7	0	0
G13	CH ₃ + CH ₂ ↔C ₂ H ₄ + H	1.807×10^7	0	0

G14	$2\text{CH}_3 \rightarrow \text{C}_2\text{H}_5 + \text{H}$	1.148×10^{15}	0	110
	reverse rate	3.674×10^7	0	0
G15	$\text{CH}_4 + \text{CH} \leftrightarrow \text{C}_2\text{H}_5$	1.626×10^8	0	0
G16	$\text{CH}_4 + \text{CH} \leftrightarrow \text{C}_2\text{H}_4 + \text{H}$	3.011×10^7	0	-1.6
G17	$\text{CH}_4 + \text{CH}_2 \leftrightarrow \text{C}_2\text{H}_6$	1.024×10^7	0	0
G18	$\text{C}_2\text{H}_3 + \text{M} \leftrightarrow \text{C}_2\text{H}_2 + \text{H} + \text{M}$	3.011×10^9	0	133
G19	$\text{C}_2\text{H}_3 + \text{H}_2 \rightarrow \text{C}_2\text{H}_4 + \text{H}$	3.011×10^{-2}	2.63	36
	reverse rate	1.325	2.53	51
G20	$\text{C}_2\text{H}_3 + \text{CH}_2 \leftrightarrow \text{C}_2\text{H}_2 + \text{CH}_3$	1.807×10^7	0	0
G21	$\text{C}_2\text{H}_3 + \text{CH}_3 \leftrightarrow \text{C}_2\text{H}_2 + \text{CH}_4$	3.914×10^5	0	0
G22	$\text{C}_2\text{H}_4 + \text{M} \leftrightarrow \text{C}_2\text{H}_2 + \text{H}_2 + \text{M}$	1.5×10^9	0	233.6
G23	$\text{C}_2\text{H}_4 + \text{M} \leftrightarrow \text{C}_2\text{H}_3 + \text{H} + \text{M}$	1.4×10^{10}	0	344.8
G24	$\text{C}_2\text{H}_4 + \text{H}_2 \rightarrow \text{C}_2\text{H}_5 + \text{H}$	1.024×10^7	0	285
	reverse rate	1.807×10^6	0	0
G25	$\text{C}_2\text{H}_4 + \text{C}_2\text{H}_2 \leftrightarrow 2\text{C}_2\text{H}_3$	2.409×10^7	0	286
G26	$2\text{C}_2\text{H}_4 \rightarrow \text{C}_2\text{H}_3 + \text{C}_2\text{H}_5$	4.818×10^8	0	299
	reverse rate	4.818×10^5	0	0
G27	$\text{CH}_4 + \text{CH}_3 \leftrightarrow \text{C}_2\text{H}_5 + \text{H}_2$	1.024×10^7	0	95.6
G28	$\text{C}_2\text{H}_5 + \text{H}_2 \rightarrow \text{C}_2\text{H}_6 + \text{H}$	3.071×10^{-6}	3.6	35
	reverse rate	1.445×10^3	1.5	31
G29	$\text{C}_2\text{H}_5 + \text{CH}_3 \leftrightarrow \text{C}_2\text{H}_4 + \text{CH}_4$	1.987×10^7	0.5	0
G30	$\text{C}_2\text{H}_6 + \text{CH}_3 \rightarrow \text{C}_2\text{H}_5 + \text{CH}_4$	0.549×10^{-3}	4	34.6
	reverse rate	8.618×10^{-8}	4.14	52.6
G31	$2\text{C}_2\text{H}_5 \leftrightarrow \text{C}_2\text{H}_6 + \text{C}_2\text{H}_4$	7.227×10^6	0	4.5
G32	$\text{C}_2\text{H}_5 + \text{C}_2\text{H}_4 \rightarrow \text{C}_2\text{H}_6 + \text{C}_2\text{H}_3$	6.624×10^{-4}	3.13	75.4
	reverse rate	6.022×10^{-4}	3.3	43.9
G33	$\text{C}_2\text{H}_2 + \text{C}_2\text{H}_6 \rightarrow \text{C}_2\text{H}_3 + \text{C}_2\text{H}_5$	104.4	2.05	292.8
	reverse rate	5.553×10^7	-0.346	46.4
G34	$\text{C}_2\text{H}_4 \rightarrow \text{C}_2\text{H}_3 + \text{H}$	4.365×10^{12}	0.945	451.6
	reverse rate	8.428×10^7	0	0
G35	$2\text{CH}_3 \rightarrow \text{CH}_2 + \text{CH}_4$	0.0152	3.153	64.6
	reverse rate	62.25	2.451	54.8
G36	$\text{CH}_2 + \text{HCl} \rightarrow \text{CH}_3 + \text{Cl}$	183.417	1.71	8.9

	reverse rate	39.6	2.24	31.8
G37	$\text{CH}_3 + \text{Cl} \rightarrow \text{CH}_2 + \text{HCl}$	2.2×10^7	0	34.5
	reverse rate	1.698×10^6	0	3.63
G38	$\text{C}_2\text{H}_5 + \text{HCl} \rightarrow \text{C}_2\text{H}_6 + \text{Cl}$	0.0123	2.29	0
	reverse rate	1.4365×10^4	1.476	8.4
G39	$\text{CH}_3 + \text{HCl} \rightarrow \text{CH}_4 + \text{Cl}$	70.106	1.412	15.7
	reverse rate	1.642×10^{-7}	4.51	5.9
G40	$\text{H}_2 + \text{H} \rightarrow 3\text{H}$	2.228×10^8	0	402
	reverse rate	9.792×10^5	-1	0
G41	$2\text{H}_2 \rightarrow 2\text{H} + \text{H}_2$	9.033×10^8	0	402
	reverse rate	9.792×10^4	-0.6	0
G42	$2\text{H} + \text{M} \leftrightarrow \text{H}_2 + \text{M}$	5.44×10^{12}	-1.3	0
G43	$\text{HCl} \rightarrow \text{H} + \text{Cl}$	1.109×10^{17}	-0.681	417.6
	reverse rate	96.39	1.87	-35.2
G44	$\text{Cl} + \text{H}_2 \rightarrow \text{HCl} + \text{H}$	7.52×10^{-4}	3.39	-4.9
	reverse rate	4.379×10^8	-0.091	35.4
G45	$\text{BCl}_3 \rightarrow \text{BCl}_2 + \text{Cl}$	5.85×10^{13}	0.31	464.1
	reverse rate	2.74×10^8	1.44	17.88
G46	$\text{CH}_4 + \text{BCl}_3 \rightarrow \text{CH}_3\text{BCl}_2 + \text{HCl}$	2.08×10^7	1.43	194.8
	reverse rate	2.4×10^8	0.5	148.4
G47	$\text{CH}_3\text{BCl}_2 \rightarrow \text{CH}_2\text{BCl}_2 + \text{H}$	1.98×10^8	1.6	348.2
	reverse rate	4.29×10^8	1.23	12.7
G48	$\text{CH}_3\text{BCl}_2 + \text{Cl} \rightarrow \text{CH}_2\text{BCl}_2 + \text{HCl}$	8.67×10^6	1.79	5.43
	reverse rate	1.76×10^6	1.78	53.0
G49	$\text{CH}_2\text{BCl}_2 \rightarrow \text{CHBCl}_2 + \text{H}$	1.5×10^{16}	-0.79	218.75
	reverse rate	6.2×10^{15}	-0.87	55.4
G50	$\text{CHBCl}_2 + \text{H} \rightarrow \text{CHBCl} + \text{HCl}$	1.05×10^9	1.36	38.58
	reverse rate	4.6×10^5	2.16	127.6
G51	$\text{CHBCl} + \text{Cl} \rightarrow \text{CBCl} + \text{HCl}$	2.67×10^{14}	-0.48	247.49
	reverse rate	6.4×10^{11}	0.048	159.2

G52	CBCl + H→CHBCl	4.58×10^{11}	0.89	2.69
	reverse rate	1.05×10^{25}	0.77	18.61
G53	CHBCl→BC + HCl	7.0×10^{13}	-0.024	30.12
	reverse rate	1.17×10^8	1.64	39.2
G54	BCl ₃ + H ₂ →BHCl ₂ + HCl	1.26×10^9	1.11	191.3
	reverse rate	2.24×10^4	2.13	99.65
G55	BHCl ₂ + H→BH ₂ Cl ₂	3.29×10^9	1.28	7.15
	reverse rate	3.52×10^{25}	0.58	0.98
G56	BH ₂ Cl ₂ →BCl ₂ + H ₂	2.25×10^{15}	-0.69	54.83
	reverse rate	6.68×10^9	0.47	64.8
G57	BCl ₂ →BCl + Cl	1.90×10^{12}	0.47	305.5
	reverse rate	1.4×10^{10}	1.13	4.14
G58	BCl + H→B + HCl	2.37×10^{12}	0.47	112.7
	reverse rate	3.27×10^{10}	1.05	4.76
G59	BCl ₃ + H→BHCl ₃	2.33×10^7	-0.54	13.23
G60	BCl ₃ + H→BHCl ₂ + Cl	2.31×10^3	1.36	44.8
G61	BCl ₃ + H→BCl ₂ + HCl	4.09×10^3	0.97	49.8
G62	BCl ₃ + H→BCl ₂ + HCl	2.6×10^4	1.23	108.4

a The rate constants are written according to Arrhenius equation: $K=ATne^{-E/RT}$. “↔” denotes the reverse rates are calculated from equilibrium thermochemistry.

2.2 Machine learning (ML)

With the great success of data-driven modeling, machine learning (ML) has received increasing attention [28-31]. Considering the production of the variety of intermediate species and the complexity of the deposition process of the CVD-B_xC, we combined a reactor model (RM) with ML, as shown in Figure 2. Considering N arbitrary samples (X_i, t_i) , where $X_i = [x_{i1}, x_{i2}, \dots, x_{in}]^T \in R^n, t_i = [t_{i1}, t_{i2}, \dots, t_{im}]^T \in R^m$. X_i represent the input

data set, and t_i is the output data set.

$$X_i = \begin{pmatrix} x_1(T), & x_1(BCl_3), & x_1(CH_4), & \cdots, & x_1(BHCl_2), \\ x_2(T), & x_2(BCl_3), & x_2(CH_4), & \cdots, & x_2(BHCl_2), \\ \cdots, & \cdots, & \cdots, & \cdots, & \cdots, \\ x_N(T), & x_N(BCl_3), & x_N(CH_4), & \cdots, & x_N(BHCl_2), \end{pmatrix}. \quad (7)$$

Error back propagation algorithm (BP) and support vector machine (SVM) are two commonly used machine learning algorithms. They have many applications in materials research [32, 33]; thus, they are applied in ML. The BP algorithm is composed of two processes: forward calculation of data stream (forward propagation) and backward propagation of error signal. In forward propagation, the propagation direction is from the input layer to the hidden layer and then to the output layer. The state of each layer of neurons only affects the next layer of neurons. However, if the actual output does not match the expected output, the process of back propagation of errors is then entered. Error backpropagation involves passing the output error back to the input layer through the hidden layer, layer by layer, apportioning the error to all units of each layer, and using the error signal obtained from each layer as the basis for adjusting the weight of each unit. Through these two processes alternately, the error function gradient descent strategy is performed in the weight vector space, and a set of weight vectors is dynamically searched to achieve the minimum network error function value. The N arbitrary samples (X_i, t_i) were entered into the BP neural algorithm program, and the specific steps are as follows:

- (1) Initialize the network, and randomly assign each connection weight $[w],[v]$ and threshold values θ_i, r_t ;
- (2) Compute hidden layers from a given input-output mode pair;
- (3) Calculate new connection weights and thresholds;
- (4) Select the next input mode pair to return to the second step, and repeat the training until the network output error reaches the required training.

The SVM algorithm is very powerful; it not only supports linear and nonlinear classification but also linear and nonlinear regression [34]. In the process of determining the hyperplane with the largest geometric interval, only the sample points closest to the hyperplane play a role. Such sample points are called support vectors.

This classification model is also called support vector machine. In practical problems, data is usually not linearly separable in a multidimensional space; that is, in the input space where the data is located, there is no hyperplane that can complete the required classification. A feasible solution is to apply kernel techniques to map data from the input space to a higher dimensional space through a specific function and look for hyperplanes in the higher dimensional space. We call this space a feature space. Because the input space is mapped to a higher dimensional feature space through specific mapping, the amount of calculation in the higher dimensional space will increase significantly, and the computational complexity will also increase significantly.

In the SVM regression, the system attempts to fit as many data as possible into the interval while limiting the margin violation. To reduce the amount of calculation, on the premise that the calculation of the support vector machine involves only the inner product calculation, a kernel function is introduced to convert the inner product calculation in the feature space into a non-linear transformation of the inner product operation of the data in the input space.

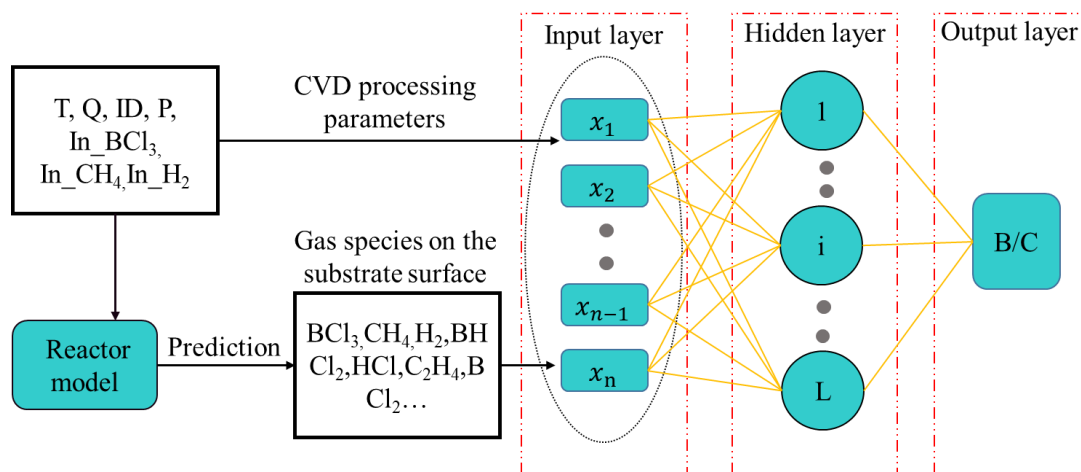


Fig 2. ML model design for B/C prediction.

It is essential to assess the error during prediction in order to evaluate the performance of BP and SVM models. This could be carried out by comparing the model predicted value and the experimentally measured values. In this regard, mean absolute percentage error (MAPE) and mean square error (MSE) were employed to assess the closeness of prediction values and measured values.

$$MAPE = \frac{100}{n} \sum_{i=1}^n \frac{|E_i - P_i|}{E_i}, \quad (8)$$

$$MSE = \frac{100}{n} \sum_{i=1}^n (E_i - P_i)^2. \quad (9)$$

where E_i is the measured experimental value; P_i indicates the ML model predicted result; and n refers to the total number of sample points.

3. Results and discussion

3.1 Temperature field distribution

The temperature distribution of the reactor is shown in Figure 3. The results show that the temperature distribution in the reactor shows a gradient distribution, and the temperature around the deposition substrate was highest, which is consistent with the actual processing temperature. The temperature distribution in the middle deposition area is relatively uniform (isothermal zone). Due to the size effect of the reactor and the cooling effect of the gas, the temperature gradient near the inlet and outlet of the isothermal zone was relatively large. The precursor was gradually heated and decomposed into a large amount of intermediate species when entering the isothermal zone, and then these intermediate species reacted on the substrate surface.

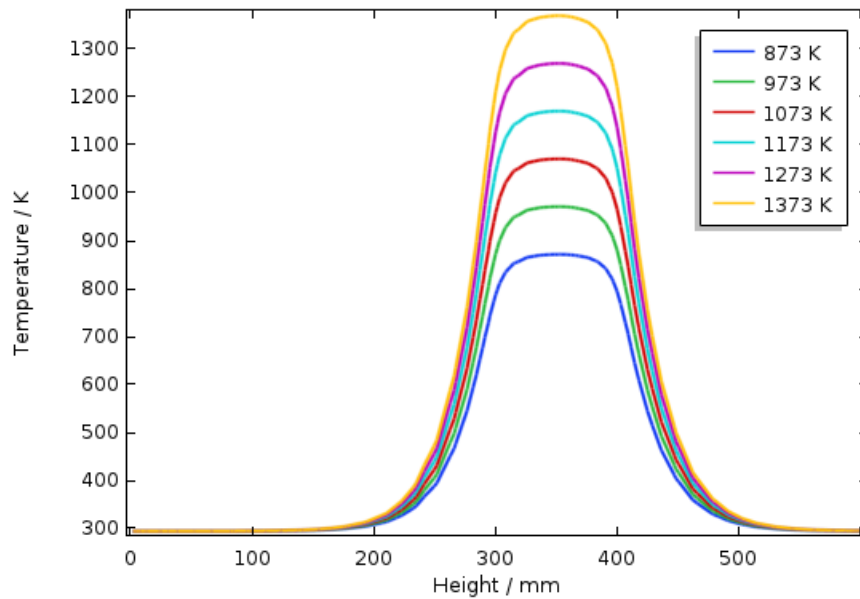


Fig 3. Axial temperature distribution curve in the reactor at different deposition temperatures.

3.2 Distribution of intermediate species

The distribution of the molar fraction of the intermediate species in the reactor is shown in Figure 4. The concentration of BCl_3 dropped sharply as it approached the substrate, which was consistent with the temperature distribution trend inside the reaction chamber. The main decomposed gas species of BCl_3 in the reaction chamber were BHCl_2 and HCl , and the trends of BHCl_2 and HCl were the same, which was consistent with the main reaction $\text{BCl}_3 + \text{H}_2 \rightarrow \text{BHCl}_2 + \text{HCl}$ [13]. BHCl_2 was considered an intermediate and/or by-product, which were formed by hydrogen reduction of BCl_3 , according to thermodynamic analysis and experimental work [13, 35]. Berjonneau et al. showed that in the case of a homogeneous reaction, CH_4 still exists in a large amount at high temperature, and in the case of a heterogeneous reaction, CH_4 will decompose to form boron carbide and graphite as a carbon source [13]. The above situation agrees with our prediction. In addition, we found that some intermediate gas phase components, such as BCl_2 , BCl , BH_2Cl_2 , CHBCl_2 , CHBCl , CH_3 , C_2H_3 , C_2H_5 , and C_2H_6 , have lower molar fractions, indicating that they do not play a dominant role in the B/C ratio of the deposited product during the homogeneous reaction.

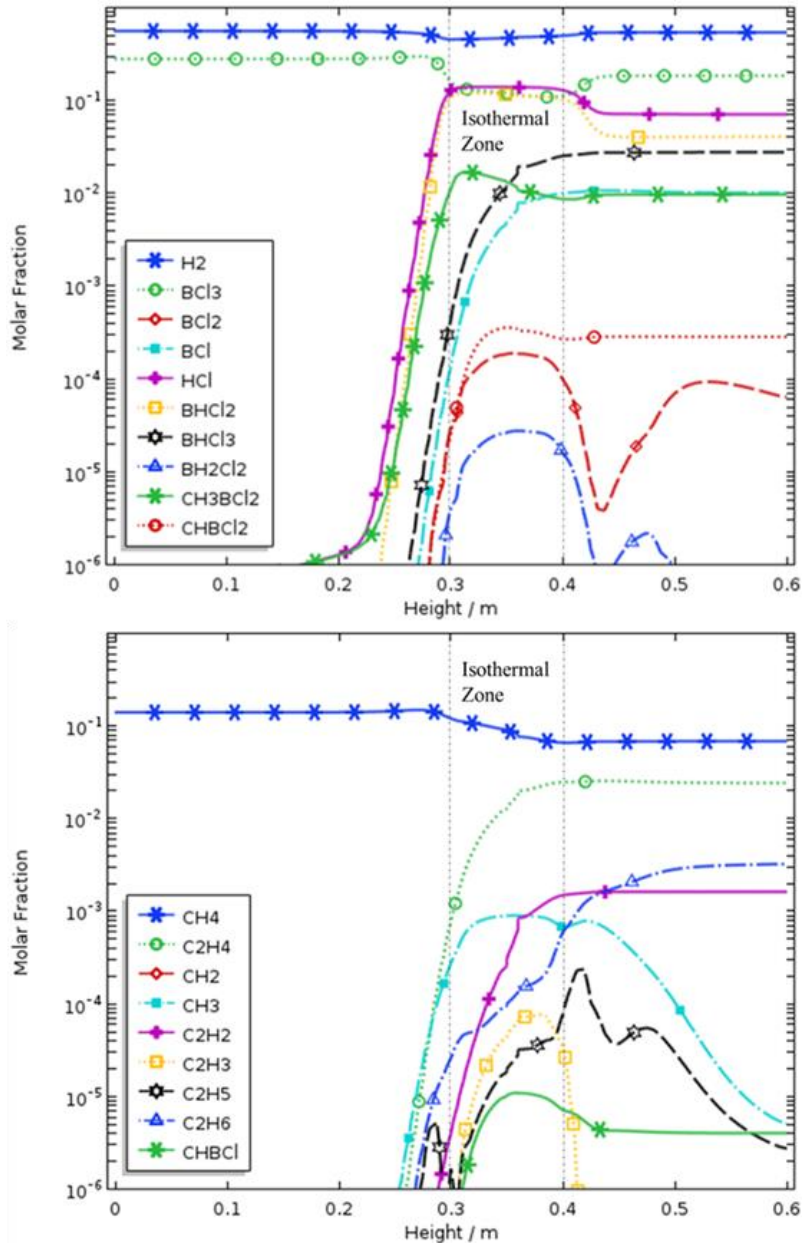


Fig 4. Plot of the gas-phase compositions along the reactor height: for deposition temperature of 1000°C, total pressure of 12 kPa, total gas flow rate of 210 sccm, In_BCl₃ is 2/7 and In_CH₄ is 1/7.

Figure 5 shows the predicted mole fractions of important species at different temperatures, with a constant feed gas composition and inlet flow rate. The concentrations are the mean values at the substrate surface. Only the major chemical species having a molar fraction larger than 10^{-4} are shown. Low temperature (900 °C) leads to less decomposition of BCl₃ and CH₄. BHCl₂ has the highest concentration, compared to other boron-containing intermediate species. The decomposition of CH₄

is very sensitive to temperature. Remarkably, at 950 °C, the concentration of hydrocarbon increased with temperature, for example, C₂H₂ and C₂H₄. The concentration of CH₄ slightly decreased with increasing temperature, and C₂H₄ became the most abundant carbon intermediate. Further, C₂H₂ became the second largest hydrocarbon species at higher temperature. The shift from CH₄ to C₂H₂ at high temperatures has also been found in hydrocarbon cracking chemistry (C-H system, without B nor Cl). These results demonstrate that the major hydrocarbon species are CH₄ and C₂H₄, and the major silicon-containing species containing boron are BCl₃, BHCl₂, BHCl₃, and CH₃BCl₂ for a typical CMC processing temperature. Our predictions are consistent with Berjonneau's experimental results and thermodynamic calculation [35].

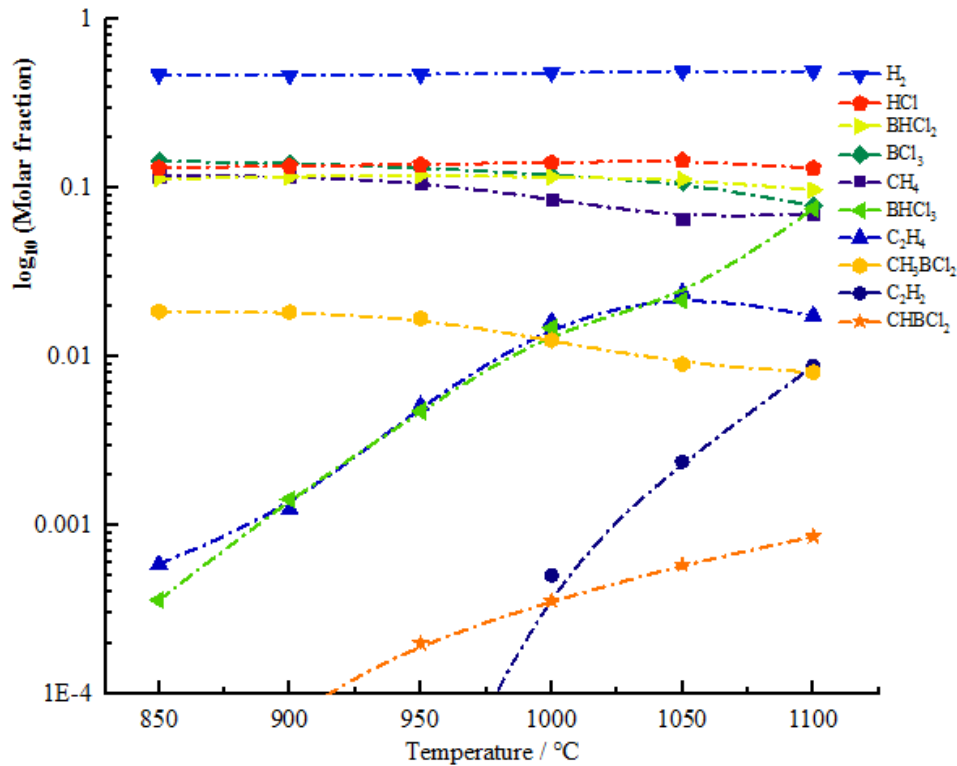


Fig 5. Influence of temperature on the mole fraction of intermediate components. total pressure of 12 kPa, total gas flow rate of 210 sccm, In_BCl₃ is 2/7 and In_CH₄ is 1/7.

3.3 Predicted boron to carbon ratio

Firstly, BP and SVM were used to directly correlate the deposition atomic ratio

with deposition conditions (temperature, input gas ratio, total pressure, reactor inner diameter and flow rate), without the reactor-scale model. Figures 6 and 8 show that the functional relationship between them is not very good ($R^2 = 0.9388$). The average values of MSE and MAPE are approximately 25% and 30%, respectively.

Next, a reactor-scale model was established to predict the molar fraction of the intermediate gas species generated in various deposition processes. Then, we used BP and SVM to relate the boron-carbon ratio values of MSE and MAPE were around 6.8% and 8.2%, respectively. Figures 7 and 9 show that the experimental measured results and predicted values are close to overlapping ($R^2 = 0.975$). As shown in Table 5, after inputting the intermediate gas species predicted by reactor-scale model into the SVM algorithm, the prediction error was reduced from 25% to 7%. Compared with the BP algorithm, the prediction of SVM was better. The prediction of SVM was determined by the algorithm itself and affected by the sample size. In the case of small sample data, SVM is recommended.

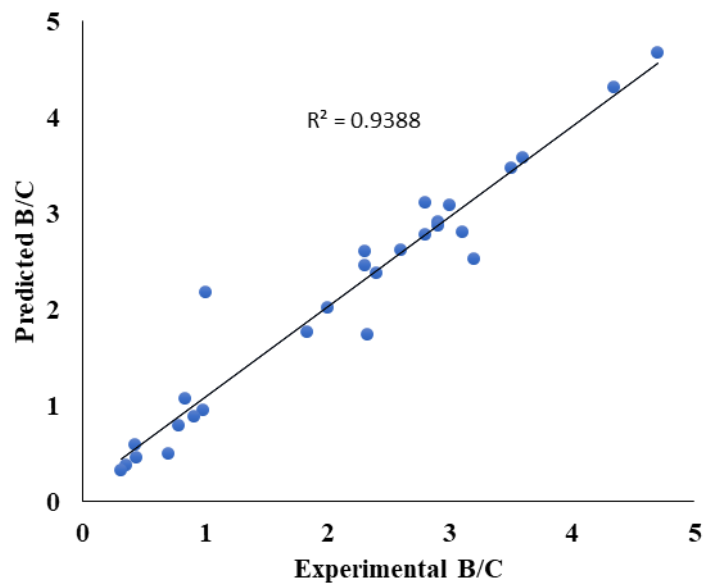


Fig 6. Goodness of fit (input variables are T, Q, P, In_BCl₃, In_CH₄, and In_H₂).

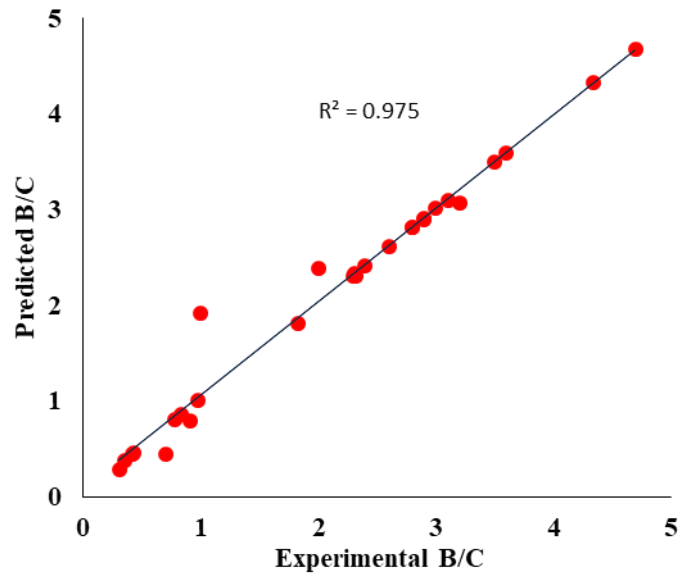


Fig 7. Goodness of fit (input variables are T, P, BCl_3 , CH_4 , BHCl_2 , BHCl_3 , BCl_2 , HCl, and H_2).

Table 5. Mean absolute percentage error and mean square error of predicted results

		SVM	BP	Average value
Without reactor-scale	MSE	16.5%	34.2%	25.35%
	MAPE	15.8%	45.6%	30.7%
With reactor-scale	MSE	1.7%	11.9%	6.8%
	MAPE	8.4%	8.1%	8.25%

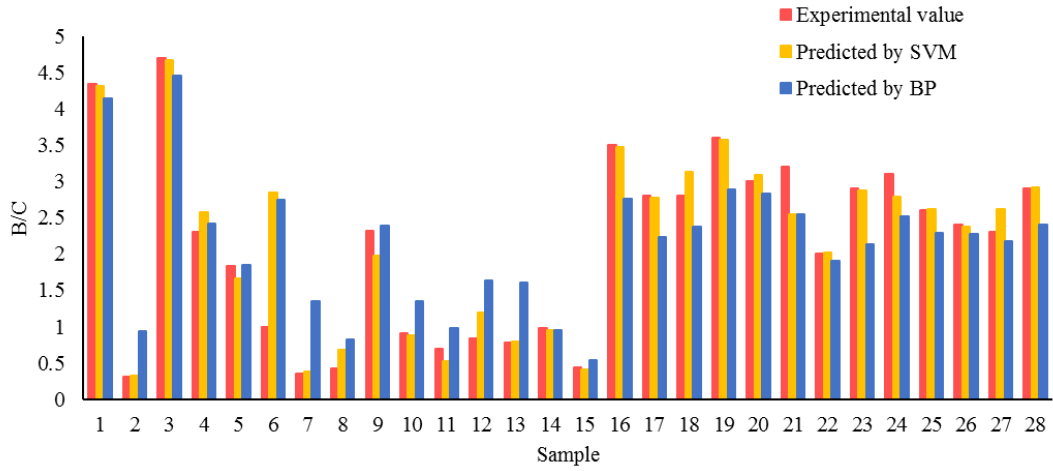


Fig 8. Predicted B/C without reactor scale (input variables are T, Q, P, ID, In_BCl₃, In_CH₄, and In_H₂)

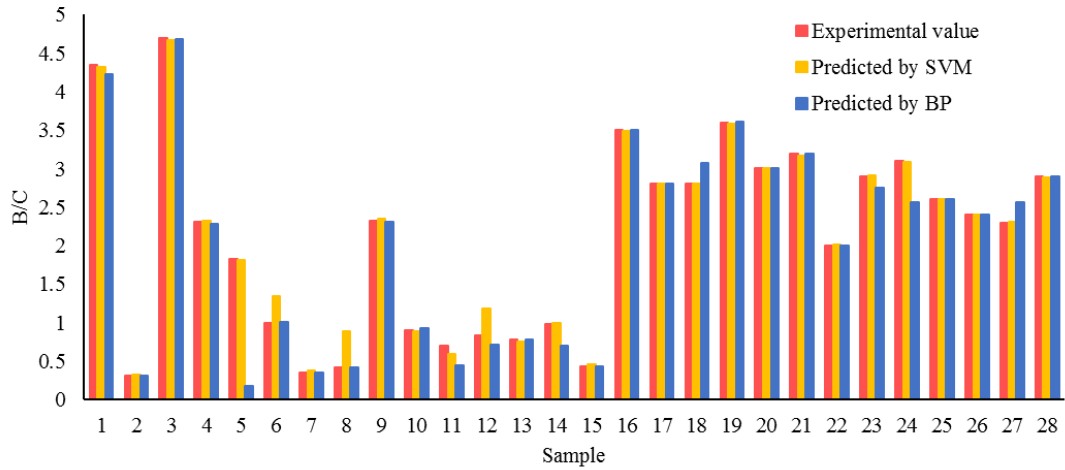


Fig 9. Predicted B/C with reactor scale (Input variables are T, P, BCl₃, CH₄, BHCl₂, BHCl₃, BCl₂, HCl, and H₂).

3.4 Sensitivity coefficient analysis

After the training session, sensitivity analysis was performed with SVM. Sensitivity coefficients were calculated with respect to the B/C:

$$S(k) = \frac{|v_0 - v|}{v} \quad (10)$$

Here, v_0 is the predicted deposition B/C by SVM training model when the molar fraction of the i th gas species is fixed as zero, and the concentrations of the other

species remain unchanged; v is the original deposition rate predicted by SVM training model. Therefore, “sensitivity” indicates the degree of influence on the predicted ratio of the components of the deposited product when the studied species is removed. Sensitivity analysis can be used to identify core species in a deposition mechanism. Obviously, a larger the $S(k)$ value for a certain substance indicates that it plays a dominant role in the deposition process.

Corresponding to 900 °C, 1000 °C, and 1100 °C, we selected samples 2, 7, and 15 to study the sensitivity coefficient. The sensitivity analysis results (Fig. 10) showed that the intermediate species with molar fractions that limit the B/C ratio are BCl_3 , CH_4 , BHCl_2 , BHCl_3 , CH_3BCl_2 , C_2H_4 , C_2H_2 , CH_4 , HCl , and H_2 . The sensitivity coefficients of other species were below 0.01, which suggests they minimally influence the B/C ratio. BHCl_2 and BCl_3 provide the most productivity for boron atoms, while C_2H_4 and CH_4 are the main sources of carbon atoms. The sensitivity coefficient of CH_4 was the largest, which is consistent with the deposition mechanism proposed by Vandenbulcke et al. [36]. Lartigue et al. also indicated that the production of CH_4 is a predominant step toward deposition [37]. The intermediate BHCl_2 was found to be very important to the deposition process, which is also consistent with Vandenbulcke’s experimental results.

To compare with the effects of boron- and carbon-containing intermediate species on the composition of deposited products, the sensitivity coefficient of the main boron- and carbon-containing intermediate species were separately calculated and then compared in Figure 11. The sensitivity coefficient of the boron-containing intermediate species increased with temperature. On the contrary, the sensitivity coefficients of carbon-containing intermediates were larger at 900 °C, and the values were higher than that of boron-containing species. This is consistent with the reported mechanism, which states that methane decomposes less as compared to boron trichloride at low temperature. This result is also consistent with the reported thermodynamic calculation results [35]. Therefore, the deposit composition is limited by methane at low temperature. At 1000 °C and 1100 °C, the decomposition of the boron- and carbon-containing intermediate species were similar, which demonstrate a

competitive deposition mechanism. Thus co-deposition occurs, and the B/C ratio of the deposits gradually decreased with temperature. We concluded the main factor controlling the boron-carbon ratio is temperature. Methane is the controlling gas species of the deposit compositions at low temperatures (~900 °C), while methane and boron trichloride both affect the deposit compositions at higher temperatures (>900 °C).

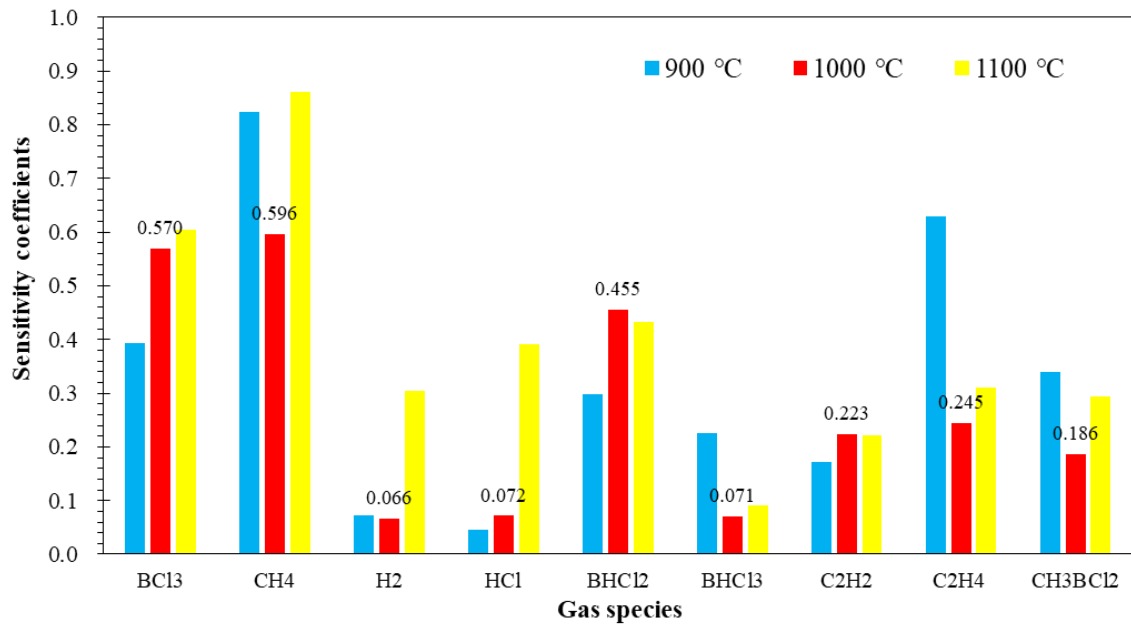


Fig 10. Analysis of the sensitivity of the intermediate species with respect to the B/C under different temperatures by ML.

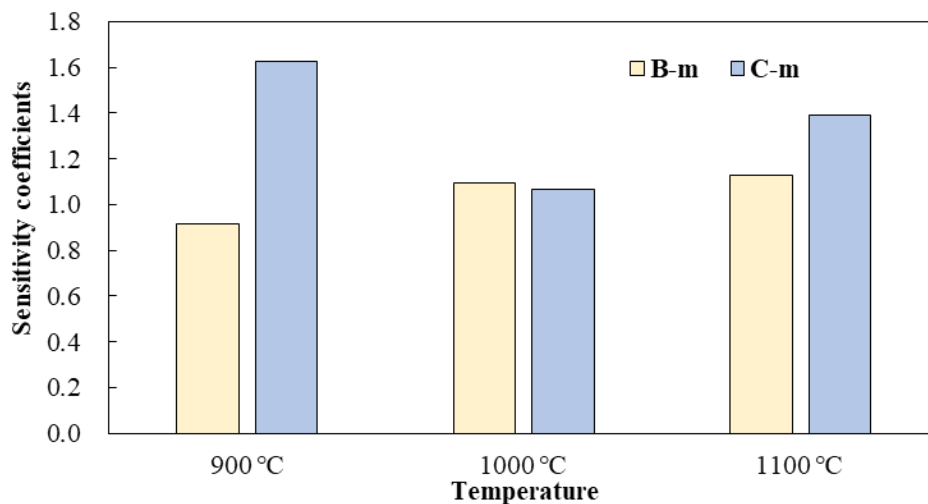


Fig 11. Analysis of the sensitivity coefficient of the main intermediate gas species containing

boron (B-m) and containing carbon (C-m) at different temperatures.

4 Conclusion

- (1) Based on the reported experimental results, we established a simplified two-dimensional reactor model, which couples gas-phase reaction, as well as heat and mass transfer, for a $\text{BCl}_3\text{-CH}_4\text{-H}_2$ system.
- (2) The main intermediate species were BCl_3 , CH_4 , BHCl_2 , BHCl_3 , CH_3BCl_2 , C_2H_4 , C_2H_2 , CH_4 , HCl , and H_2 , and the changes in BHCl_2 and HCl were the same. This result was consistent with the main reaction $\text{BCl}_3 + \text{H}_2 \rightarrow \text{BHCl}_2 + \text{HCl}$.
- (3) Comparing machine learning techniques without reactor-scale model, the prediction error of machine learning techniques incorporated with reactor-scale model was reduced from 25% to 7%.
- (4) Sensitivity analysis shows that, with the exception of temperature, CH_4 is the key factor in controlling the deposit compositions at low temperature, while CH_4 and BCl_3 are both important at high temperature.

In summary, the combination of reactor model and machine learning allows for the prediction of the boron-carbon ratio of the deposited product within a reasonable error range (less than 10%). This method can also be applied to other multi-element CVD systems.

Acknowledgement

We thank the National Key R&D Program of China (Grants No. 2017YFB0703200), National Natural Science Foundation of China (Grants No. 51702100, 51972268) and China Postdoctoral Science Foundation (Grants No. 2018M643075) for financial support.

References

- [1] Ohnabe H, Masaki S, Onozuka M, et al. Potential Application of Ceramic Matrix Composites to Aero-Engine Components. *Compos Part A-Appl S* 1999, **30**: 489-96.
- [2] Naslain R, Guette A, Rebillat F, et al. Boron-bearing species in ceramic matrix composites

for

long-term aerospace applications. *J Solid State Chem* 2004, **30**: 489-96.

- [3] Christin F. Design, fabrication, and application of thermostructural composites (TSC) like C/C, C/SiC, and SiC/SiC composites. *Adv Eng Mater* 2002, **4**: 903-12.
- [4] Katoh Y, Snead LL, Henager CH, et al. Current status and recent research achievements in SiC/SiC composites. *J Nucl Mater* 2014, **455**: 387-97.
- [5] Inghels E, Lamon J. An approach to the mechanical behaviour of SiC/SiC and C/SiC ceramic matrix composites. *J Mater Sci* 1991, **26**: 5411-9.
- [6] Liu YS, Cheng LF, Zhang LT, et al. Oxidation protection of multilayer CVD SiC/B/SiC coatings for 3D C/SiC composite. *Mat Sci Eng A-Struct* 2007 **466**: 172-7.
- [7] Sezer AO, Brand JI. Chemical vapor deposition of boron carbide. *Mater Sci Eng B-Adv* 2001 **79**: 191-202.
- [8] Jacques S, Guette A, Langlais F, et al. C(B) materials as interphases in SiC/SiC model microcomposites. *J Mater Sci* 1997.
- [9] Ruggles-Wrenn MB, Wallis TA. Creep in interlaminar shear of an Hi-Nicalon™/SiC-B₄C composite at 1300°C in air and in steam. *J Compos Mater* 2019, **54**: 1819-29.
- [10] Deshpande SV, Gulari E, Harris SJ, et al. Filament activated chemical vapor deposition of boron carbide coatings. *Appl Phys Lett* 1994, **65**: 1757-9.
- [11] Karaman M, Sezgi NA, Doğu T, et al. Kinetic investigation of chemical vapor deposition of B₄C on tungsten substrate. *AICHE J* 2006, **52**: 4161-6.
- [12] Karaman M, Sezgi NA, Doğu T, et al. Mechanism studies on CVD of boron carbide from a gas mixture of BCl₃, CH₄, and H₂ in a dual impinging-jet reactor. *AICHE J* 2009, **55**: 701-9.
- [13] Berjonneau J, Langlais F, Chollon G, et al. Understanding the CVD process of (Si)-B-C ceramics through FTIR spectroscopy gas phase analysis. *Surf Coat Tech* 2017, **201**: 7273-85.
- [14] Berjonneau J, Chollon G, Langlais F, et al. Deposition process of Si-B-C ceramics from CH₃SiCl₃/BCl₃/H₂ precursor. *Thin Solid Films* 2008, **516**: 2848-57.
- [15] Liu YS, Zhang LT, Cheng LF, et al. Uniform design and regression analysis of LPCVD boron carbide from BCl₃-CH₄-H₂ system. *Appl Surf Sci* 2009, **255**: 5729-35.
- [16] Zeng B, Feng ZD, Li SW, et al. Microstructural study of oxidation of carbon-rich amorphous boron carbide coating. *Front Mater Sci* 2008, **2**: 375-80.
- [17] Mollick PK, Venugopalan R, Srivastava D. CFD coupled kinetic modeling and simulation of hot wall vertical tubular reactor for deposition of SiC crystal from MTS. *J Cryst Growth* 2017, **475**: 97-109.
- [18] Ni H, Lu S, Chen C. Modeling and simulation of silicon epitaxial growth in siemens cvd reactor. *J Cryst Growth* 2014, **404**: 89-99.
- [19] Deck CP, Khalifa HE, Sammuli B, et al. Fabrication of SiC-SiC composites for fuel cladding in advanced reactor designs. *Prog Nucl Energy* 2012, **57**: 38-45.
- [20] Li J, Qin H, Liu Y, et al. Effect of the SiCl₄ flow rate on SiBN deposition kinetics in SiCl₄-BCl₃-NH₃-H₂-Ar environment. *Materials* 2017, **10**: 627.
- [21] Cuadros F, Cachadiña I, Ahumada W. Determination of Lennard-Jones interaction parameters using a new procedure. *Mol Eng* 1996, **6**: 319-25.

- [22] Ge Y, Gordon M S, Battaglia F, et al. Theoretical study of the pyrolysis of methyltrichlorosilane in the gas phase. 1. Thermodynamics. *J Phys Chem A* 2007, **111**: 1462-74.
- [23] Ge Y, Gordon M S, Battaglia F, et al. Theoretical study of the pyrolysis of methyltrichlorosilane in the gas phase. 2. Reaction paths and transition states. *J Phys Chem A* 2007, **111**: 1475-86.
- [24] Ge Y, Gordon M S, Battaglia F, et al. Theoretical study of the pyrolysis of methyltrichlorosilane in the gas phase. 3. Reaction Rate Constant Calculations. *J Phys Chem A* 2010, **114**: 2384-92.
- [25] Yan L, Su K, Zeng Q, et al. Reaction paths of $\text{BCl}_3 + \text{CH}_4 + \text{H}_2$ in the chemical vapor deposition process. *Struct Chem* 2012, **23**.
- [26] Liu Y, Su K, Zeng Q, et al. Decomposition reaction rate of $\text{BCl}_3\text{-CH}_4\text{-H}_2$ in the gas phase. *Theor Chem Acc* 2015, **134**.
- [27] Reinisch G, Leyssale J M, Vignoles G L. Theoretical study of the decomposition of BCl_3 induced by a H radical. *J Phys Chem A* 2011, **115**: 4786-97.
- [28] Lee J H, Shin J, Realf M J. Machine learning: Overview of the recent progresses and implications for the process systems engineering field. *Comput Chem Eng* 2018, **114**: 111-21.
- [29] Moreno R, Corona F, Lendasse A, et al. Extreme learning machines for soybean classification in remote sensing hyperspectral images. *Neurocomputing* 2014, **128**: 207-16.
- [30] Basu A, Shuo S, Zhou H, et al. Silicon spiking neurons for hardware implementation of extreme learning machines. *Neurocomputing* 2013, **102**: 125-34.
- [31] Benoît F, Heeswijk M, Miche Y, et al. Feature selection for nonlinear models with extreme learning machines. *Neurocomputing* 2013, **102**: 111-24.
- [32] Feng S, Zhou H, Dong H, et al. Using deep neural network with small dataset to predict material defects. *Mater Des* 2019, **162**: 300-10.
- [33] Kushvaha V, Kumar S A, Madhushri P, et al. Artificial neural network technique to predict dynamic fracture of particulate composite. *J Compos Mater* 2020.
- [34] Liu X, Gao C, Li P, et al. A comparative analysis of support vector machines and extreme learning machines. *Neural Netw* 2012, **33**: 58-66.
- [35] Berjonneau J, Chollon G, Langlais F, et al. Deposition process of amorphous boron carbide from $\text{CH}_4/\text{BCl}_3/\text{H}_2$ precursor. *Proceedings Electrochemical Society* 2006, **153**: C795-C800.
- [36] Vandenbulcke L G. Theoretical and experimental studies on the chemical vapor deposition of boron carbide. *Ind Eng Chem Res* 2002, **24**: 568-75.
- [37] Lartigue S, Cazajous D, Nadal M, et al. Study of boron carbides vapor-deposited under low pressure. In: In proceedings of the fifth European conference on chemical vapor deposition. Uppsala. Sweden: Uppsala University, Department of Chemistry. 1985: 413-9.